飞秒激光成丝的衍射分析方法

郑恒毅[1,2]，尹富康[1,2]，王铁军[1,2*]，刘尧香[1]，魏迎霞[1]，朱斌[3]，周凯南[3]，冷雨欣[1,2]

[1]中国科学院上海光学精密机械研究所强场激光物理国家重点实验室，上海 201800；

[2]中国科学院大学材料与光电研究中心，北京 310027；

[3]中国工程物理研究院激光聚变研究中心等离子体物理重点实验室，四川 绵阳 621999

摘要　提出了一种用于模拟探测光穿过等离子体通道后衍射成像过程的分段衍射模型，该模型考虑了等离子体对探测光的散焦效应。将分段衍射模型与现有计算模型进行对比，并将模拟结果与基于纵向衍射测量法的实验结果进行拟合，获得了不同衍射环结构下的电子密度分布。结果表明：分段衍射模型可以拓展探测范围，实现对较高电子密度等离子体的测量。基于分段衍射模型测量电子密度和光丝尺寸的方法为精确诊断光丝提供了一种新思路。

关键词　非线性光学；飞秒激光成丝；等离子体诊断；衍射理论；电子密度

中图分类号　O436　　　**文献标志码**　A　　　　　　　　　　　**DOI**：10.3788/CJL202249.2408001

1　引　　言

强飞秒激光在空气等透明介质中传播时，若光克尔自聚焦效应与中性分子电离产生的等离子体散焦效应之间达到了动态平衡，飞秒激光就会在介质中形成等离子体通道，即成丝现象[1-4]。飞秒激光成丝在引导控制放电[5-7]、遥感探测[8-10]、太赫兹辐射[11-14]和超短脉冲压缩[15-16]等领域显示出了极大的应用潜力。光丝尺寸及其内部电子密度的测量对于理解光丝的传输和演化规律、开展各项应用都具有重要意义。一般来说，光丝内电子密度的测量通常可以分为两大类。其中的一类探测方法，如电学测量法[17]、声学测量法[18]和荧光测量法[19]等，相对来说要简单易行一些，但是若要获得电子密度的绝对值则需要定标，并且精度有限，不具有时间分辨的能力；另一类方法，如利用干涉[20-22]、衍射[23-26]和全息[27-29]实现密度测量的方法，在实验设置上都具有泵浦探测的实验结构，这类方法通过等离子体所引起的探测光的相位改变量提取出电子密度，同时可以通过调节泵浦光和探测光的时间延时获得电子密度的时空演化信息。利用干涉原理相对来说能获得更精确的电子密度分布，尤其是沿光丝轴向的密度分布，但为了获得干涉条纹，需要将探测光分成两束并进行准确调节使其时空同步，从而增加了实验操作的复杂性。纵向衍射法的实验光路相对来说更简单，可以在牺牲轴向分辨信息的情况下观测到等离子体密度随时间的演化。

在已有的基于纵向衍射法的工作中[19,24,26]，研究人员所使用的探测光衍射传播模型有一定的局限性，即：当电子密度并不是非常高（$<10^{17}$ cm^{-3}）或者等离子体通道不是很长时，通道内的电子导致的探测光的偏折可以忽略。因此，他们假设探测光沿轴向穿过光丝后，等离子体的散焦效应只改变了探测光复振幅的相位项，即只引起了一个与电子密度有关的额外的常数相移。但实际上，探测光的光强分布会受到等离子体散焦效应的调制，尤其是当等离子体密度较高时，这种调制更是不可忽略的，否则会影响提取到的电子密度和光丝直径的准确性。本课题组根据标量衍射理论建立了分段衍射成像模型，以精确模拟探测光的衍射传播过程，并以该模型为基础对实验记录的衍射图像进行拟合，提取出了电子密度和光丝尺寸信息。该模型不仅适用于模拟较低电子密度下的衍射情况，同时也适用于电子密度较高时需要考虑光丝散焦效应的情况。

2　基本理论

纵向衍射法的光路模型如图 1 所示。当一束探测光穿过预先形成的等离子体通道时，由于等离子体区域的折射率小于周围空气的折射率，等离子体对探测光相位的调制引起的散焦效应会使探测光在远端的像面上呈现衍射环结构的强度分布。其中光丝的长度为 L_{fil}，透镜到光丝和成像面的距离分别为 L_1 和 L_2。下面对探测光的衍射传播过程进行模拟分析。
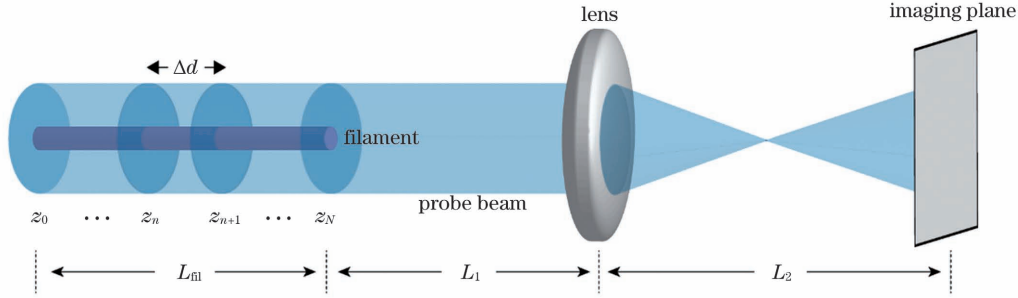
图 1 探测光被光丝衍射后成像的计算模型图

Fig. 1 Computational model diagram of probe beam diffracted by filament

标量衍射理论可以有效描述自由空间中光的传输过程，它是对光的传输效应的一个合理近似[30-31]。菲涅耳衍射积分[30-32]通常是模拟衍射过程的首选方法，因为它适用的传输场景比较广泛，且在计算上相对简单直观。它可以表示为

$$U_2(x,y) = \iint U_1(\xi,\eta) h(x-\xi, y-\eta) \, d\xi d\eta, \quad (1)$$

其中

$$h(x,y) = \frac{\exp(jkz)}{j\lambda z} \exp\left[\frac{jk}{2z}(x^2+y^2)\right], \quad (2)$$

即输出面光场的复振幅 U_2 是输入面光场的复振幅 U_1 与脉冲响应 $h(x,y)$ 的卷积，其中 z 是传输距离，λ 为光波长，$k=2\pi/\lambda$。当光经过一个薄透镜时，忽略透镜的尺寸，紧靠透镜之前的平面上的光场 $U_{l'}(x,y)$ 和入射到紧靠透镜之后的平面上的光场 $U_l(x,y)$ 之间的关系[30]可以写成

$$U_l(x,y) = U_{l'}(x,y)\exp\left[-j\frac{k}{2f}(x^2+y^2)\right]. \quad (3)$$

式(3)表明焦距为 f 的薄透镜起到了一个相位变换的作用。等离子体通道的折射率 n 和电子密度 n_e 的关系[21]可以表示为

$$n = \left(1 - \frac{n_e}{n_c}\right)^{\frac{1}{2}} \approx 1 - \frac{n_e}{2n_c}, \quad (4)$$

式中：n_c 是等离子体的临界密度，对于波长为 400 nm 的探测光，$n_c = 6.88 \times 10^{21}$ cm^{-3}。假设光丝中的电子密度呈柱对称分布，并且在光丝的径向方向上呈高斯分布，即

$$n_e(r) = n_{e0}\exp(-r^2/w^2), \quad (5)$$

式中：n_{e0} 是峰值电子密度；w 为高斯分布的 1/e 半径；r 为柱坐标系的坐标，$r = \sqrt{x^2+y^2}$。因此，当探测光穿过光丝时产生的空间相移也呈沿径向的高斯分布，可记为

$$\varphi_{fil}(r) = -k\Delta d \frac{n_{e0}}{2n_c}\exp(-r^2/w^2), \quad (6)$$

式中：Δd 是探测光在光丝中传输的距离。可以看到，虽然式(6)是使用折射率的近似式推导得到的，但是由于光丝中的电子密度一般远小于等离子体的临界密度，所以使用近似式引入的相位变化将远小于等离子体自身引起的相位变化。

在当前现有的研究[19,24,26]中，研究人员假设探测光的初始复振幅分布为 $U_{in} = \exp(-ar^2)$，经等离子体通道调制后，通道出口处的复振幅分布为 $U_{out} = \exp(-ar^2)\exp[j\varphi(r)]$，其中 $\varphi(r) = -k[n_e/(2n_c)]L_{fil}$ 是整段光丝引起的总相移，a 是探测光束腰半径平方的倒数，然后根据标量衍射理论计算得到像面上的光强分布。他们在计算过程中认为探测光在等离子体通道入口和出口处的光强分布是相同的，同时假设低密度等离子体的散焦效应只体现在相位改变上。当电子密度较高且径向梯度变化较大时，该假设会使电子密度的精确测量变得困难[24]。为了获得相对更准确的衍射结果，使纵向衍射法在较高电子密度下仍能实现较精确的测量，本课题组利用下面的计算过程模拟探测光在等离子体通道中的散焦效应。如图 1 所示，等离子体通道被等分成 N 段，每段的长度为 $\Delta d = L_{fil}/N$，探测光在光丝入口处($z = z_0$)的复振幅分布为 $U_0 = \exp(-ar^2)$。将探测光在每一段所经历的散焦调制都视为只有相位发生改变，先用式(1)计算得到探测光在 Δd 距离内的衍射传输结果，然后乘以该段光丝引起的相移 $\exp[j\varphi_{fil}(r)]$，相乘的结果即为该段最终的光场分布，同时也是下一段传输过程的初始平面的复振幅分布。将这一过程重复 N 次后，最终得到光丝出口处的复振幅分布 $U_{L_{fil}}$。该计算流程如图 2 所示。然后继续利用式(1)和式(3)计算得到探测光经透镜传播到像面的光场分布。为了说明不同分段数 N 对最终结果的影响，这里以电子密度分布 $n_{e0} = 6.9 \times 10^{17}$ cm^{-3}、$w = 45$ μm 的高斯分布为例计算了不同分段数目下的光强，其中光丝长度 L_{fil} 假设为 1 cm，透镜到光丝和成像面的距离分别为 41 cm 和 45 cm，透镜焦距为 20 cm。图 3 显示了分段数 N 分别等于 0(即不分段，把光丝对探测光的影响视为只产生了额外相移)、5、25、50 时探测光在光丝出口[图 3(a)]和成像位置[图 3(b)]处的径向光强分布。可以看到：当对光丝分段之后，位于光丝出口处的光强分布体现出了等离子体散焦效应的影响，中心区域的光强降低；当光丝未分段时，光丝出口处的光强没有体现出散焦效应，并且计算得到的位于成像端的衍射条纹强度分布明显偏离分段后的结果。随着分段数增加($N \geq 25$)，光丝出口处和像面上的光强分布趋于稳定。图 3(c)和图 3(d)分别是分段数取 25 时模拟得到的光丝出口处和成像平面上的光强分布。
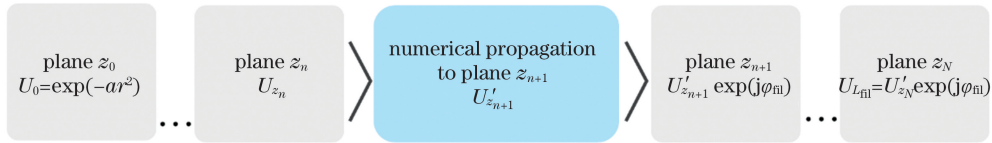
图 2 探测光在等离子体通道中传输时的计算流程图

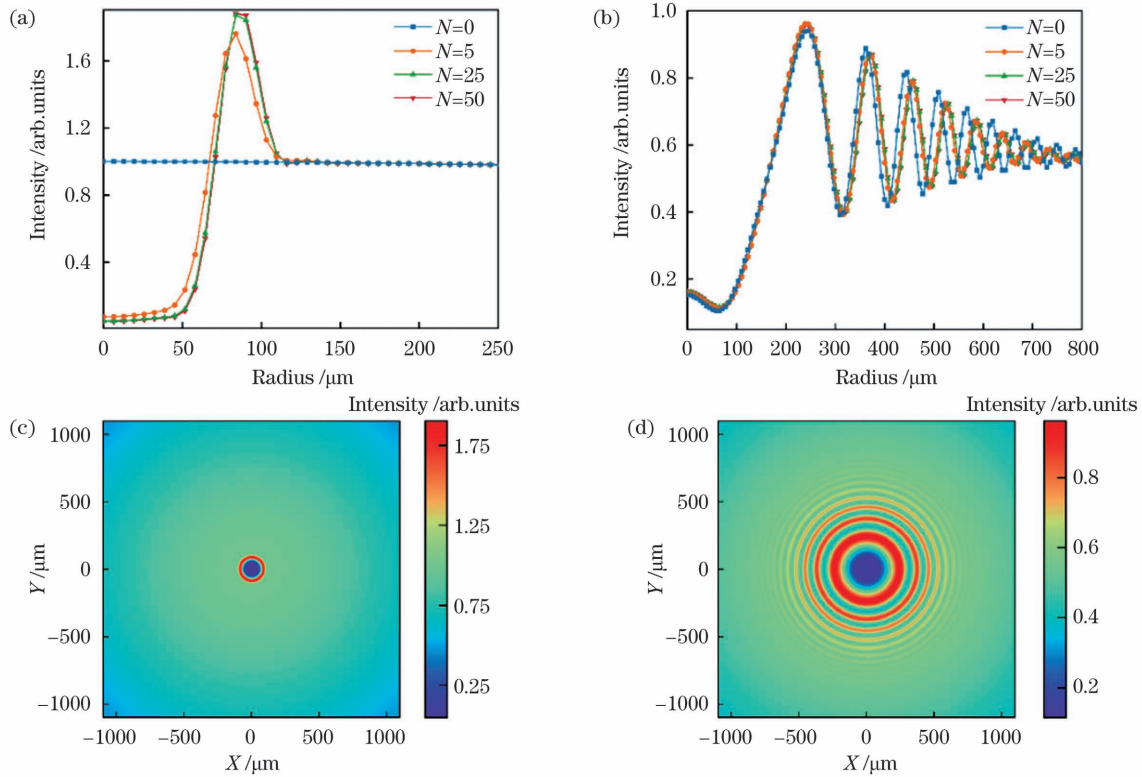Fig. 2 Computation flow chart when probe beam propagates in plasma channel

图 3 探测光强度分布的模拟结果。不同分段数下探测光的径向强度分布：（a）光丝出口处；（b）CCD 成像端。分段数为 25 时的平面光强分布：（c）光丝出口处；（d）CCD 成像端

Fig. 3 Simulation results of intensity distribution of probe beam. Radial intensity distribution of probe beam at different numbers of segments：(a) at the exit of filament；(b) at CCD imaging end. Plane intensity distribution when the number of segments is 25：(c) at the exit of filament；(d) at CCD imaging end

3 拟合与分析

将模拟结果与实验值进行拟合，可以提取出电子密度分布和光丝尺寸的信息。实验中成丝所用的泵浦激光的中心波长为 800 nm，脉宽为 30 fs，脉冲重复频率为 50 Hz。泵浦激光经焦距为 30 cm 的正透镜聚焦成丝，成丝前泵浦光脉冲能量为 4.5 mJ，根据荧光测得光丝的长度约为 1 cm。波长为 400 nm 的探测光由飞秒激光倍频得到，可以调节其与泵浦光之间的延时。用 CCD 记录探测光的衍射像。由前述可知，模拟得到的衍射条纹分布受每一段光丝产生的相移的影响，即与式（6）中的 n_{e0} 和 w 相关。当改变 n_{e0} 和 w 时，衍射环的结构会发生相应的变化。增大峰值电子密度可使较高级次的衍射环强度增大，进而使得衍射环的数目变多；而增大光丝半径会使中心区域受到的调制增强，高级次的衍射环强度减弱，且沿径向衰减得更快。此外，衍射环的半径始终随着 n_{e0} 和 w 的增大而增大。为了便于后续的拟合，将计算中光场平面的采样间隔

设置成与 CCD 像元尺寸一致，均为 6.45 μm，且预先对模拟和实验得到的强度值均沿着径向取平均并分别进行归一化处理。首先改变初始变量 n_{e0} 和 w，计算得到一系列不同的像面衍射强度分布；然后将每一个模拟结果都与实验结果进行比较，判断拟合的接近程度，提取出对应的 n_{e0} 和 w。当前有关纵向衍射法的研究对于拟合过程的描述比较模糊，而且对于模拟结果是否达到最佳拟合状态的判断具有一定的主观性。本文通过计算二者的误差平方和（SSE）来寻找最合适的拟合状态。则，对于第 i 个模拟结果有

$$S_i = \sum_{j=1}^{n} (I_{ij} - I'_j)^2, \tag{7}$$

式中：S_i 表示第 i 个模拟结果的 SSE；I_{ij} 表示第 i 个模拟结果沿径向第 j 个点处的强度值；I'_j 表示实验结果沿径向第 j 个点处的强度值。当 SSE 取最小值时，即可根据对应的 n_{e0} 和 w 获得电子密度分布和光丝尺寸。
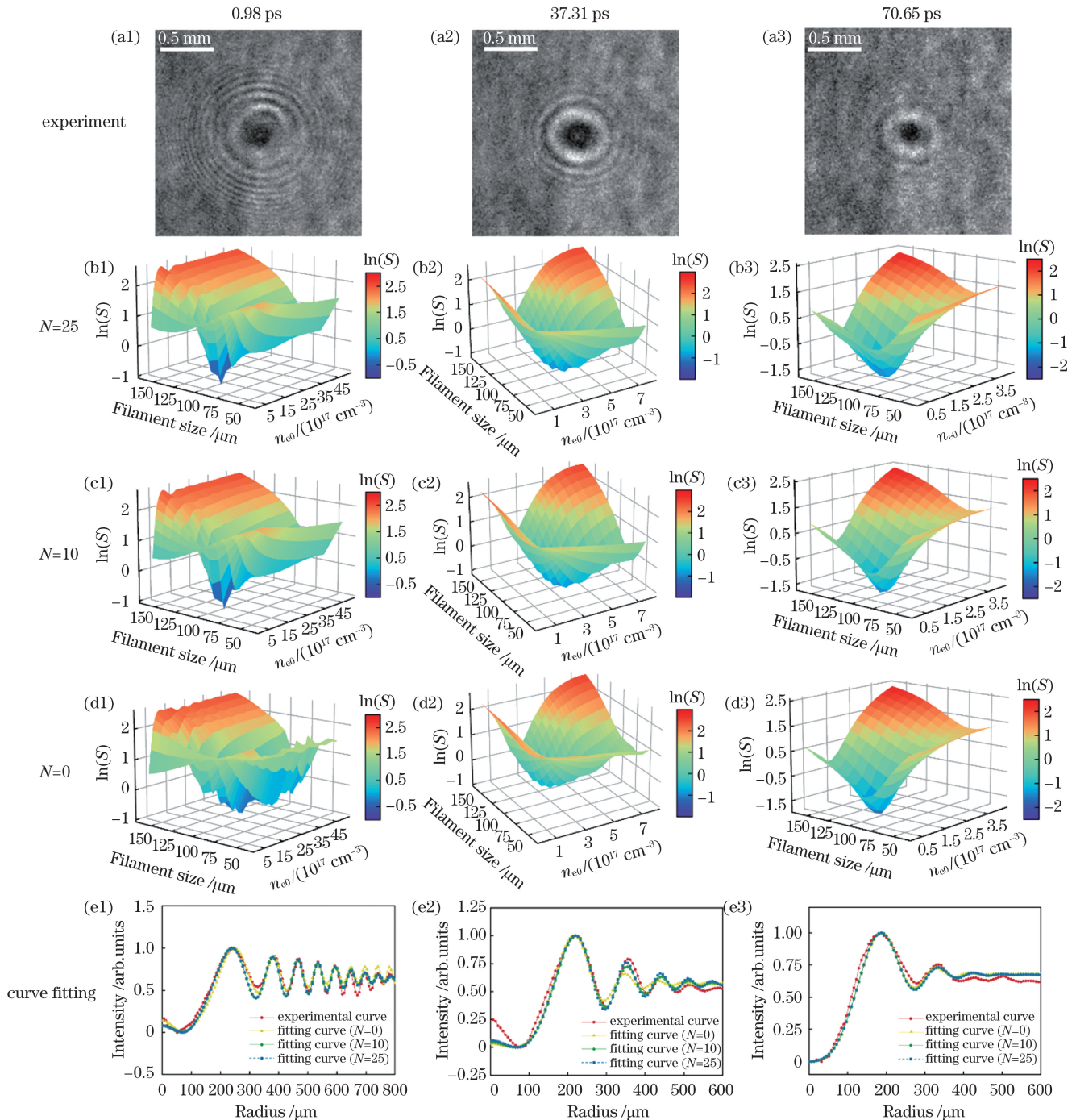
依照上述拟合过程，分别选取分段数 N 为 25、10 和 0，对实验记录的衍射圆环进行拟合。图 4（a1）为探

图 4　不同延时下的模拟和计算结果。(a1)~(a3)CCD 记录的不同时刻的衍射环；(b1)~(d3)不同延迟和分段数下 SSE 计算值的分布图；(e1)~(e3)拟合结果

Fig. 4　Simulated and calculated results at different delays. (a1)−(a3) Diffraction patterns at different delays recorded by CCD; (b1)−(b3) distribution maps of calculated SSE values at different delays and segments; (e1)−(e3) fitting results

测光相对于成丝光的延时为 0.98 ps 时 CCD 端记录的衍射图样。可以看到，在较高脉冲能量和紧聚焦的成丝条件下，早期较高密度的等离子体通道体现出了对探测光强烈的衍射调制。将计算得到的不同峰值电子密度(n_{e0})和光丝尺寸($2w$)组合下的 SSE 取对数值，结果如图 4(b1)~(d3)所示。由图 4(b1)和图 4(c1)可知，当采用分段衍射模型计算时，$N=25$ 和 $N=10$ 下的 SSE 对数曲面图产生了一个显著的凹陷区域，该凹陷区域的最小值均在(n_{e0}，$2w$)=($8.8×10^{17}$ cm^{-3}，

90 μm)处取得，对应的拟合结果如图 4(e1)所示。当分段数 N 为 0 时，等离子体散焦效应只体现在额外的相移上，SSE 的最小值对应的最优解为(n_{e0}，$2w$)=($2.1×10^{18}$ cm^{-3}，90 μm)，且该 SSE 值比基于分段衍射模型得到的结果更大，说明对应的拟合效果要劣于使用分段模型得到的结果。另外可以看到，不分段时得到的曲面图并未产生一个明显的凹陷区域，这意味着该最小值并不具有显著优势，对应的电子密度分布也不是一个准确可靠的结果。故，当电子密度比较高

时，若假设探测光只是发生了相移变化，就会使衍射强度分布与实际情况有较大偏差，难以实现对电子密度和光丝直径的精确测量。随着等离子体密度衰减，衍射效应逐渐减弱，图 4(a2)~(e2) 为 37.31 ps 延时情况下的拟合和计算结果。从 SSE 分布图中提取出的最优解分别为 $(3.9 \times 10^{17} \text{ cm}^{-3}, 90 \text{ } \mu\text{m})$、$(3.6 \times 10^{17} \text{ cm}^{-3}, 100 \text{ } \mu\text{m})$ 和 $(3.0 \times 10^{17} \text{ cm}^{-3}, 120 \text{ } \mu\text{m})$。尽管在该延时下基于直接添加相移模型计算得到的 SSE 分布图存在凹陷区域，但其 SSE 最小值仍大于分段衍射模型的结果，且图 4(e2) 所示的拟合曲线与实际情况存在更大的偏差。这进一步说明了分段衍射模型在拟合效果上更优异，提取的电子密度分布相对更准确。当延迟达到 70.65 ps 时，如图 4(a3) 所示，衍射效应进一步减弱，此时 N 为 25、10 和 0 下的对数曲面图均产生了一个明显的凹陷，凹陷区域对应的最优解分别为 $(1.4 \times 10^{17} \text{ cm}^{-3}, 100 \text{ } \mu\text{m})$、$(1.4 \times 10^{17} \text{ cm}^{-3}, 100 \text{ } \mu\text{m})$ 和 $(1.7 \times 10^{17} \text{ cm}^{-3}, 110 \text{ } \mu\text{m})$。拟合结果如图 4(e3) 所示，两个模型的测量结果相差不大，且均能够较好地拟合实验结果。这说明当电子密度下降到 $1 \times 10^{17} \text{ cm}^{-3}$ 左右时，将光丝对探测光的散焦效应假设成一个额外的相移是比较合理的，这与 Liu 等[24] 的研究结果一致。从衍射的角度看，当假设电子密度呈柱对称分布时，探测光穿过等离子体通道受到的调制作用不是单纯的相位调制，而是复振幅整体都受到了调制。直接添加相移模型对于这一调制过程的考虑是不完善的，会影响后续自由传播成像的计算，最终导致像面光场分布计算结果的准确度下降，对实验的拟合效果不佳。分段衍射计算能够体现出光场复振幅整体受到调制的过程，使用分段计算能够模拟给出探测光被调制后的复振幅分布，拟合误差更小，可以更准确地获得光丝内电子密度沿径向的空间分布。

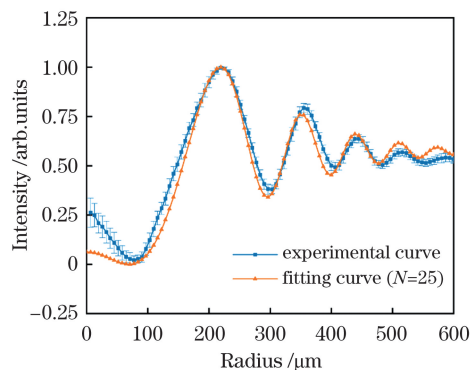图 5 中的实验曲线是对同一延时下的 30 幅衍射图统计分析后的结果。可见，径向强度分布比较稳定，与实验自身误差相比，拟合曲线与实验曲线之间的误差更大。实际的电子密度分布可能并不完全满足柱对

称的高斯分布，因而会产生拟合误差，影响电子密度反演结果的精确性。然而，根据 SSE 的最小值拟合的衍射结构的强度变化趋势与实验结果基本相符，提取的电子密度值 $(10^{17} \sim 10^{18} \text{ cm}^{-3})$ 与已有的基于电导率法[17]、荧光法[19]、全息法[27] 的测量结果基本一致，证实了本文所提模型对电子密度分布的衍射测量和分析计算具有较高的准确性。

4 结　　论

本课题组提出了一个基于标量衍射理论的分段衍射计算模型，并将其用于模拟探测光在与光丝同向传播时被等离子体通道衍射调制的过程。基于该模型对实验记录的探测光衍射环进行了拟合，以模拟结果与实验结果之间的 SSE 为判断标准，获得最合适的拟合结果，进而提取出对应的峰值电子密度和光丝直径。将分段衍射模型与当前研究中使用的直接添加相移的模型进行了对比，结果表明：分段衍射模型不仅适用于较低电子密度分布的测量与提取，同时也适用于电子密度较高、衍射效应较强的情况；直接添加相移的模型在较高电子密度情况下的测量结果偏差较大。分段衍射模型拓展了纵向衍射法的测量范围，为不同电子密度条件下等离子体通道的精确衍射测量提供了新思路。

图 5　实验测量误差与拟合误差的比较

（延时为 37.31 ps）

Fig. 5　Comparison of experimental measurement error and fitting error (delay time is 37.31 ps)

参 考 文 献

[1] Chin S L. Filamentation physics[M]//Springer series on atomic, optical, and plasma physics. New York: Springer, 2009, 55: 11-48.

[2] Bergé L, Skupin S, Nuter R, et al. Ultrashort filaments of light in weakly ionized, optically transparent media[J]. Reports on Progress in Physics, 2007, 70(10): 1633-1713.

[3] Kasparian J, Wolf J P. Physics and applications of atmospheric nonlinear optics and filamentation[J]. Optics Express, 2008, 16(1): 466-493.

[4] 刘伟伟, 薛嘉云, 苏强, 等. 超快激光成丝现象研究综述[J]. 中国激光, 2020, 47(5): 0500003.
Liu W W, Xue J Y, Su Q, et al. Research progress on ultrafast laser filamentation[J]. Chinese Journal of Lasers, 2020, 47(5): 0500003.

[5] Rodriguez M, Sauerbrey R, Wille H, et al. Triggering and guiding megavolt discharges by use of laser-induced ionized filaments[J]. Optics Letters, 2002, 27(9): 772-774.

[6] Clerici M, Hu Y, Lassonde P, et al. Laser-assisted guiding of electric discharges around objects[J]. Science Advances, 2015, 1(5): e1400111.

[7] Wang T J, Wei Y X, Liu Y X, et al. Direct observation of laser guided corona discharges[J]. Scientific Reports, 2016, 5: 18681.

[8] Kasparian J, Rodriguez M, Méjean G, et al. White-light filaments for atmospheric analysis[J]. Science, 2003, 301(5629): 61-64.

[9] Luo Q, Xu H L, Hosseini S A, et al. Remote sensing of pollutants using femtosecond laser pulse fluorescence spectroscopy[J]. Applied Physics B, 2006, 82(1): 105-109.

[10] 王铁军, 陈娜, 郭豪, 等. 飞秒强激光大气遥感新技术的原理和研究进展[J]. 激光与光电子学进展, 2022, 59(7): 0700001.
Wang T J, Chen N, Guo H, et al. Principle and research progress of atmospheric remote sensing by intense femtosecond

lasers[J]. Laser & Optoelectronics Progress, 2022, 59(7): 0700001.

[11] Xie X, Dai J M, Zhang X C. Coherent control of THz wave generation in ambient air[J]. Physical Review Letters, 2006, 96(7): 075005.

[12] Kim K Y, Taylor A J, Glownia J H, et al. Coherent control of terahertz supercontinuum generation in ultrafast laser‐gas interactions[J]. Nature Photonics, 2008, 2(10): 605-609.

[13] Wang T J, Yuan S, Chen Y P, et al. Toward remote high energy terahertz generation[J]. Applied Physics Letters, 2010, 97(11): 111108.

[14] 惠雨晨, 赵佳宇. 外电场作用下飞秒激光成丝辐射太赫兹波的全电流模型[J]. 光学学报, 2022, 42(1): 0114002.
Hui Y C, Zhao J Y. Full current model for terahertz wave generation from femtosecond laser filament under external electric fields[J]. Acta Optica Sinica, 2022, 42(1): 0114002.

[15] Hauri C P, Kornelis W, Helbing F W, et al. Generation of intense, carrier-envelope phase-locked few-cycle laser pulses through filamentation[J]. Applied Physics B, 2004, 79(6): 673-677.

[16] 冯天利, 商景诚, 李涛. 基于双光成丝过程的光参量啁啾脉冲放大器前端[J]. 中国激光, 2022, 49(7): 0708002.
Feng T L, Shang J C, Li T. Front-end of optical parametric chirped-pulse amplifier based on dual laser filamentation[J]. Chinese Journal of Lasers, 2022, 49(7): 0708002.

[17] Abdollahpour D, Suntsov S, Papazoglou D G, et al. Measuring easily electron plasma densities in gases produced by ultrashort lasers and filaments[J]. Optics Express, 2011, 19(18): 16866-16871.

[18] Yu J, Mondelain D, Kasparian J, et al. Sonographic probing of laser filaments in air[J]. Applied Optics, 2003, 42(36): 7117-7120.

[19] Théberge F, Liu W W, Simard P T, et al. Plasma density inside a femtosecond laser filament in air: strong dependence on external focusing[J]. Physical Review E, 2006, 74(3): 036406.

[20] Clark T R, Milchberg H M. Time- and space-resolved density evolution of the plasma waveguide[J]. Physical Review Letters, 1997, 78(12): 2373-2376.

[21] Yang H, Zhang J, Li Y J, et al. Characteristics of self-guided laser plasma channels generated by femtosecond laser pulses in air[J]. Physical Review E, 2002, 66(1): 016406.

[22] Wahlstrand J K, Chen Y H, Cheng Y H, et al. Measurements of the high field optical nonlinearity and electron density in gases: application to filamentation experiments[J]. IEEE Journal of Quantum Electronics, 2012, 48(6): 760-767.

[23] Tzortzakis S, Prade B, Franco M, et al. Time-evolution of the plasma channel at the trail of a self-guided IR femtosecond laser pulse in air[J]. Optics Communications, 2000, 181(1/2/3): 123-127.

[24] Liu J S, Duan Z L, Zeng Z N, et al. Time-resolved investigation of low-density plasma channels produced by a kilohertz femtosecond laser in air[J]. Physical Review E, 2005, 72(2): 026412.

[25] Rodriguez G, Valenzuela A R, Yellampalle B, et al. In-line holographic imaging and electron density extraction of ultrafast ionized air filaments[J]. Journal of the Optical Society of America B, 2008, 25(12): 1988-1997.

[26] Zhang Z, Lu X, Xi T T, et al. Long distance filamentation of 400 nm femtosecond laser pulses in air[J]. Applied Physics B, 2009, 97(1): 207-213.

[27] Centurion M, Pu Y, Liu Z W, et al. Holographic recording of laser-induced plasma[J]. Optics Letters, 2004, 29(7): 772-774.

[28] Abdollahpour D, Papazoglou D G, Tzortzakis S. Four-dimensional visualization of single and multiple laser filaments using in-line holographic microscopy[J]. Physical Review A, 2011, 84(5): 053809.

[29] Petrov N V, Putilin S E, Chipegin A A. Time-resolved image plane off-axis digital holography[J]. Applied Physics Letters, 2017, 110(16): 161107.

[30] Goodman J W. Introduction to Fourier optics[M]. 4th ed. San Francisco: McGraw-Hill, 2017.

[31] Voelz, David G. Computational Fourier optics: a MATLAB tutorial[M]. Bellingham: SPIE, 2011.

[32] Khare K. Fresnel and Fraunhoffer diffraction[M]//Fourier optics and computational imaging. Chichester: John Wiley & Sons, Inc., 2015: 153-165.

Diffraction Analysis of Femtosecond Laser Filaments

Zheng Hengyi[1,2], Yin Fukang[1,2], Wang Tiejun[1,2*], Liu Yaoxiang[1], Wei Yingxia[1], Zhu Bin[3], Zhou Kainan[3], Leng Yuxin[1,2]

[1] *State Key Laboratory of High Field Laser Physics, Shanghai Institute of Optics and Fine Mechanics, Chinese Academy of Sciences, Shanghai 201800, China;*
[2] *Center of Materials Science and Optoelectronics Engineering, University of Chinese Academy of Sciences, Beijing 100049, China;*
[3] *Laser Fusion Research Center and Science & Technology on Plasma Physics Laboratory, China Academy of Engineering Physics, Mianyang 621999, Sichuan, China*

Abstract

Objective　Femtosecond laser filamentation has garnered significant attention and shown great potential in guiding discharge and remote sensing detection owing to its unique characteristics. The measurement of the size and internal electron density of a filament is of great significance for understanding the nonlinear propagation and evolution law of a filament and for developing various applications. Electron density measurements in a filament can be divided into two categories: direct measurement detection method such as electrical measurement and measurement of the density by interference, diffraction, and holography. The experimental setup of the longitudinal diffraction method is relatively simple, and the temporal evolution of plasma density can be recorded at the expense of axial resolution information. However, the diffraction propagation models of probe beam based on the longitudinal diffraction method in previous studies ignored the modulation of the probe beam intensity affected by plasma defocusing. Modulation from the plasma defocusing

effect cannot be ignored when the plasma density is high. In this study, a segmented diffraction imaging model based on scalar diffraction theory is established to accurately simulate the diffraction transmission process of a probe beam.

Methods   Scalar diffraction theory effectively describes the propagation of light in free space and is a reasonable approximation of the propagation effect of light. In this work, a plasma channel was divided equally into N segments; the length of each segment was $\Delta d = L_{fil}/N$, and the complex amplitude distribution of the probe beam at the entrance of the filament ($z = z_0$) was $U_0 = \exp(-ar^2)$. The defocusing modulation experienced by the probe beam in each section was regarded only as a phase change. The calculation process is illustrated in Figure 2. First, the diffraction transmission result of the probe beam at a distance was calculated using equation (1). Second, the result of the first step was multiplied by the phase shift caused by this section of the filament. The result of the second step was the final light-field distribution in this section and the complex amplitude distribution of the initial plane of the next transmission process. Finally, the first and second steps were repeated N times, and the complex amplitude distribution at the exit of the filament was obtained. A comparison was made between the segmented diffraction model and previous models.

Results and Discussions   The structure of the diffraction ring changes correspondingly with changes in n_{e0} and w. The intensity of higher-order diffraction rings and the number of diffraction rings increase with an increase in the electron density. The modulation of the central region is enhanced, and the intensity of the high-order diffraction rings is weakened with an increase in the filament radius. Additionally, the radius of the diffraction rings always increases with an increase in n_{e0} and w. Under the conditions of high pulse energy and tight focusing, the early high-density plasma channel shows strong diffraction modulation for the probe beam [Figure 4(a1)]. The SSE logarithmic surfaces with $N = 25$ and $N = 10$ produce a significant depression area, and the minimum values in the depression are obtained at (n_{e0}, $2w$) = (8.8 × 10^{17} cm^{-3}, 90 μm) using the segmented diffraction model. The corresponding fitting results are shown in Figure 4(e1). The plasma defocusing effect is only reflected in the additional phase shift, and the optimal solution corresponding to the minimum value of the SSE is (n_{e0}, $2w$) = (2.1 × 10^{18} cm^{-3}, 90 μm) with the number of segments $N = 0$. The SSE value of segment $N = 0$ is larger than that based on the segment diffraction model. This indicates that the corresponding fitting effect of segments $N = 0$ is worse than that of the segmented model. The surface obtained without segmentation does not produce a prominent concave region; therefore, the minimum value is insignificant and the corresponding electron density distribution is not accurate and reliable. The probe beam is only subject to a change in the phase shift, and the diffraction intensity distribution deviates greatly from the actual situation. It is difficult to accurately measure the electron density and diameter of a filament with a relatively high electron density. The SSE value of segments $N = 0$ is also larger than the result based on the segment diffraction model under the relatively low electron density condition [Figure 4(e2)]. The measurement results of the two models are similar, and both fit the experimental results well when the electron density drops to approximately 1×10^{17} cm^{-3}. The plasma channel is assumed to have a cylindrical symmetric electron density distribution. The modulation effect of the probe beam passing through the plasma channel is not a simple phase modulation but a complex amplitude modulation. The consideration of directly adding a phase-shift model to this modulation process is imperfect. The segmented diffraction calculation reflects the process by which the complex amplitude of the light field is modulated as a whole. The segmented calculation simulates the distribution of the complex amplitude of the modulated probe beam with a smaller fitting error. Correspondingly, the radial spatial distribution of the electron density of the filament can be obtained more accurately. The radial intensity distribution of the experimental curve is relatively stable. The radial intensity variation trend of the diffraction structure fitted according to the minimum value of the sum variance SSE is consistent with the experimental results. The calculation method based on subsection diffraction is reasonable and reliable for the diagnosis and estimation of electron density distribution.

Conclusions   A piecewise diffraction calculation model based on scalar diffraction theory was proposed to simulate the propagation of probe beam in the same direction as the filament. Based on this model, the diffraction rings of the detected light recorded in the experiment were fitted. The results show that the segmented diffraction model can extend the measurement range for higher electron densities. The measurements of the electron density and filament size based on the segmented diffraction model provide a new analysis method for the precise diagnosis of filaments.

Key words   nonlinear optics; femtosecond laser filament; plasma diagnosis; diffraction theory; electron density